Compacting an assembly of soft balls far beyond the jammed state: Insights from three-dimensional imaging

Jonathan Barés,[1,*] Manuel Cárdenas-Barrantes,[2,†] Gustavo Pinzón,[3,‡] Edward Andò,[4,§] Mathieu Renouf,[1,‖] Gioacchino Viggiani,[3,¶] and Emilien Azéma[1,5,**]

[1]*LMGC, Université de Montpellier, CNRS, Montpellier, France*
[2]*CFTC, Universidade de Lisboa, 1749-016 Lisbonne, Portugal*
[3]*Université Grenoble Alpes, Grenoble INP, CNRS, 3SR, 38000 Grenoble, France*
[4]*EPFL Center for Imaging, École Polytechnique Fédérale de Lausanne, Lausanne 1015, Switzerland*
[5]*Institut Universitaire de France, Paris, France*

(Received 25 May 2023; accepted 2 October 2023; published 23 October 2023)

Very soft grain assemblies have unique shape-changing capabilities that allow them to be compressed far beyond the rigid jammed state by filling void spaces more effectively. However, accurately following the formation of these systems by monitoring the creation of new contacts, monitoring the changes in grain shape, and measuring grain-scale stresses is challenging. We developed an experimental method that overcomes these challenges and connects their microscale behavior to their macroscopic response. By tracking the local strain energy during compression, we reveal a transition from granular-like to continuous-like material. Mean contact geometry is shown to vary linearly with the packing fraction, which is supported by a mean field approximation. We also validate a theoretical framework which describes the compaction from a local view. Our experimental framework provides insights into the granular micromechanisms and opens perspectives for rheological analysis of highly deformable grain assemblies in various fields ranging from biology to engineering.

DOI: 10.1103/PhysRevE.108.044901

I. INTRODUCTION

Compressing a disordered assembly of grains is a seemingly simple process that has been carried out since the dawn of time by humanity to store, transport, or transform matter. The objectives are quite basic: either to improve the strength of the resulting material or to optimize space by reducing the volume taken by the grains. In the most common case of hard grains (i.e., grains with high stiffness relative to the applied pressure P), the compression generally ends once the grains can no longer rearrange, meaning a mechanically stable state is reached unless grains break. This so-called jammed state [1–3] mainly depends on the grain morphologies (size [4] and shape [5,6]), the friction between them [5], and the loading process [2]. The packing fraction ϕ cannot exceed that of the random close packing (RCP), and the coordination number Z (i.e., the average number of contacts per grain) cannot be higher than 6 for spherical (12 for nonspherical) grain assemblies. It is well documented that the applied stresses are transmitted by an inhomogeneous network of forces in which only a small proportion of grains bears the strongest forces [7,8]. The elastic properties of the assembly, around the jammed state, cannot be directly deduced from grains elasticity and result from a subtle intertwining between the values of the packing fraction, the coordination number, and contact properties [9–11]. The same is true for the coordination number, which evolves as a power law of the packing fraction [12–14].

But what if we consider soft and even squishy grains [15] (i.e., grains having a low stiffness relatively to the applied pressure) while continuing to compress the packing? The grains would deform, changing their shapes elastically or in a more complex manner, without breaking to accommodate for the internal mechanical and geometrical constraints. As a result, the solid fraction would exceed that of the RCP, and it would even be possible to entirely fill the space. A new world, as yet poorly understood, is opening up with these materials made of soft, squishy, deformable grains. Such materials play a major role in various fields of natural sciences (foams, colloidal suspensions, biological cells, blood clogging in a vein, etc.) and in many industrial processes (emulsions, metallic powders, sintered material, rubber mixtures, etc.). In soft granular assemblies, the macro- and microscale behaviors are no longer uniquely ruled by the steric exclusions and the topological disorder of contacts but are also ruled by the bulk behavior of each constitutive grain. Including the change in grain shape in addition to the inherently multicontact nature of a granular system in realistic three-dimensional (3D) modeling is a vast emerging topic, with challenging experimental, numerical, and theoretical issues [15,16].

From a numerical point of view, these last few years have seen the advent of new strategies in the form of discrete element methods coupled with different continuum approaches

*jonathan.bares@umontpellier.fr
†macardenasb@fc.ul.pt.
‡gustavo.pinzon-forero@insa-lyon.fr.fr
§edward.ando@epfl.ch
‖mathieu.renouf@umontpellier.fr
¶cino.viggiani@3sr-grenoble.fr
**emilien.azema@umontpellier.fr

[15]. Although technical challenges still remain, especially in terms of computational time, existing studies, mainly in two dimensions and a few in three dimensions [17–19], have allowed us to glimpse new microscopic mechanisms that take place from contact scale to the inside of the grains. For example, the power-law dependence of the coordination number on the packing fraction is still valid far beyond the jammed state [20–24], even for assemblies of initially noncircular grains [25]. Local grain rearrangements, sometimes dramatic, can still occur even after the jamming point [26–29], but at the same time the stress distribution becomes more homogeneous as the packing fraction increases. Friction also contributes to a better homogenization of the contact force network [25]. By implementing some of these new microscopic descriptors into a rigorous micromechanical framework, Cantor *et al.* (in two dimensions [22]) and Cárdenas-Barrantes *et al.* (in two [24,30] and three [23] dimensions) stated compaction equations fully determined by the evolution of the microstructure, thus resolving a long-standing issue verified by the very large number of *ad hoc* models that have been proposed over the last few decades [21,31–35].

Still, there is no experimental validation, especially in three dimensions, of all these advances. Even more important, no clear strategies exist to explore highly deformable granular systems far beyond the jammed state from the particle scale. More generally, whether it is in two or three dimensions, the measurement of contacts (position and orientation) and forces or stresses in the grains, as well as the description of their evolution, is mostly based on inverse problem methods. Close to the jammed state it is always assumed that the contacts obey a Hertz type law [36]. It is then possible to detect the contacts and to extrapolate the resulting interaction forces using different local field measurements such as the deformation of the grain [37,38], a photoelastic [39,40] or thermoelastic [41] signal, and raw measurements from digital image correlation [42]. These inverse methods have also been successfully extended to two-dimensional (2D) noncircular grains assemblies [43,44] and also to 3D analysis using x-ray tomography with different granular materials [45]. Careful image analysis work has also allowed some inroads into the problem [46].

Far from the jammed point, at least two challenging issues appear: (i) Hertz's law is no longer valid, and (ii) it is difficult to follow the shape of the particles while detecting new contacts. This last point is particularly exacerbated in three dimensions and at large packing fraction since it requires high image resolution. Moreover, it is not always possible to use a direct optical approach to measure local particle properties, and nontrivial tomographic reconstructions may be necessary. Most 3D experimental studies based on highly deformable, squishy grains are macroscopic and focus on general properties such as stress release [47,48], seismic isolation [49,50], and foundation damping [51]. To the best of our knowledge, only the work of Mukhopadhyay and Peixinho in 2011 [52], using fluorescent hydrogel spheres, associated with a tomographic reconstruction, was able to follow the local evolution of compressed packing up to a density of 0.85. In particular, they described the evolution of particle connectivity, but unlike what was obtained numerically, they did not report power-law dependences between the coordination number and packing fraction.

In this work, we present a 3D experimental technique that measures the displacement field directly at the grain scale (within grains), without any material or geometrical assumptions. This is performed by combining advanced digital volume correlation (DVC) methods together with accurate x-ray tomography imaging. This method is applied to the paradigmatic case of axial compression with prevented radial strain: a cylindrical sample containing 60 bidisperse silicone beads with diameters of 3 and 4 mm is compressed vertically. Micrometer-scale glass beads are trapped in the particle material to form a 3D homogeneous random pattern to facilitate DVC. The granular medium is quasistatically compressed in an x-ray scanner to obtain density images of the evolving system, halting loading during scans. Experiments were repeated four times. The major outcome of this work is the simultaneous measurement of the topological (contacts and shapes) and bulk (internal strain fields) properties of each grain throughout the whole compression process up to a very high packing fraction. This permits the inference of the grain-scale stress tensors from the loading history and the material rheology. In a context where 3D simulations are still rare and highly demanding in terms of time, our method allows the description of the microstructural and micromechanical properties of any squishy granular system deep in the jammed state. This allows validation and extension to uniaxial compression constitutive laws recently introduced numerically and in 2D configurations [22,23] in view of theoretical modeling.

II. EXPERIMENTAL METHOD

A. Sample preparation and *in situ* compression

The granular samples are made of 60 silicone beads, 24 with a diameter of 4 mm and 36 with a diameter of 3 mm (see Fig. 1). These particles are molded with SORTA-Clear 18 silicone by Smooth-On [53], mixed with glass beads with diameters between 40 and 70 μm that make up 35% in mass. The silicone is viscous enough for the glass beads not to sediment during polymerization. Just before molding, the silicone is degassed to remove air bubbles. Each grain is coated with talc powder to avoid the particles sticking together. They end up having a friction coefficient of 0.59 ± 0.15. Young's modulus of the material is $E = 0.663$ MPa, and its Poisson ratio is $\nu = 0.289$.

To account for the variability of the initial state, four independent experiments are performed. Each specimen is prepared by placing particles individually and layer by layer inside an oedometer 15 mm in diameter. To avoid segregation and crystallization effects, each "layer" consists of two large and three small particles. The particles are deposited until the height of the assembly reaches 15 mm, yielding a specimen aspect ratio of 1. The oedometer is then closed and mounted on top of the rotation stage of the x-ray tomography cabin, built by RX Solutions [54]. The loading system is located below the setup; thus, the loading is applied from the lower plate of the oedometer. The oedometric compression is performed "*in situ*," i.e., imaging the specimen while performing the test step by step: the specimen is compressed at a loading speed of 4 μm, using displacement steps of 250 μm, after which the loading system is paused and the specimen is imaged. To perform a scan, three x-ray projections are averaged for

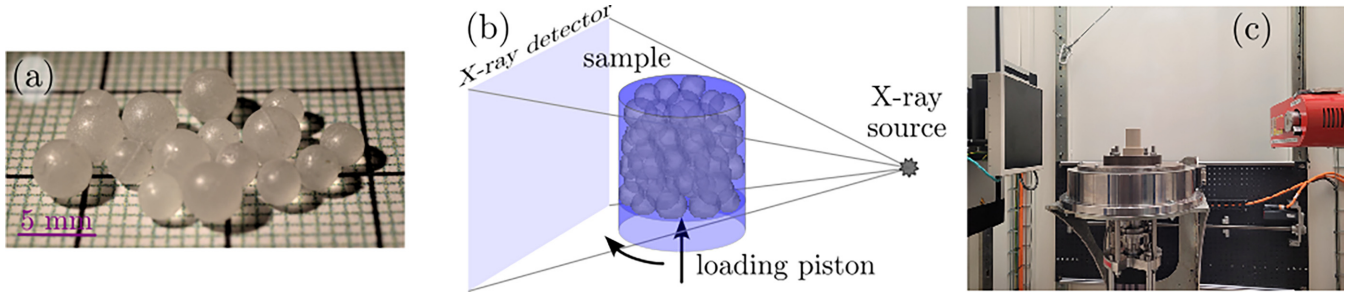

FIG. 1. (a) Picture of the custom-made silicone particles. The large particles are 4 mm wide, while the small ones have a diameter of 3 mm. (b) Schematic view of the *in situ* uniaxial compression setup. (c) Picture of the experimental setup.

each of the 1120 different radial positions, and a 3D field is reconstructed using the filtered back-projection algorithm proposed in [55], as implemented within the X-ACT software provided by RX Solutions, saved on a 16-bit data range. The x-ray tomography scans are performed using a pixel size of 15 μm/pixel, resulting in more than 200 pixels per particle diameter. The loading force is measured externally, and each specimen is compressed until a packing fraction of $\phi \approx 1$ is reached.

B. Numerical method for postprocessing

From each experiment we obtain about twenty-five 16-bit density matrices of dimension $1200 \times 1200 \times 1800$. We first convert the matrices into 8 bits. Then we isolate the large cluster of connected grains from the rest of the system on the initial undeformed image by means of thresholding. Eroding this cluster sequentially, we isolate the centers of the grains. To segment grains in the initial image we detect voxels on the borders of this large cluster containing all the grains. Considering these voxels one by one, we check whether the lines going from it to the two closest particle centers stay included in the cluster. If so, that means the voxel belongs to a contact border. These voxels forming penny shaped clusters give the border of the contact, where we have to separate particles. We look for the planes in which each of these clusters is included and cut the big cluster of grains along these planes. As shown in Fig. 2(c), we obtain the clusters of voxels covering each particle.

From the initial particle clustering, regular cubic meshes are built inside each grain. They form a network of correlation cell centers that will be tracked from one image to the next all along the compression. The distance between the nodes of this network is 12 voxels. From one image to the next, the solid rigid motion of each grain is first computed: on the first image, around the closest correlation cell center from the particle center of mass, a cubic submatrix with a side of 36 voxels is extracted. By means of Fourier transformation it is convolved with the submatrix at the same location in the next image. The position of the maximum of convolution gives the particle translation with voxel accuracy. To improve this displacement measurement, we minimize the squared difference between the first submatrix and the second one deformed by a first order shape function: $f(x, y, z) = x_0 + \alpha_x x + \beta_x y + \gamma_x z, _0 + \alpha_y x + \beta_y y + \gamma_y z, z_0 + \alpha_z x + \beta_z y + \gamma_z z$. Once the solid rigid motion of each particle is obtained, by applying the same process as the one described for the particle center of mass to each correlation cell center we obtain the displacement field inside each particle. In this computation step, the correlation cell size is 18 voxels, and if the correlation criterion is low enough, then the shape function is just a translation. The process is sequentially repeated for each consecutive pair of images.

From the displacement field obtained from DVC, the displacement of the particle borders is deduced, and the evolution of the particle shapes is tracked along the compression pro-

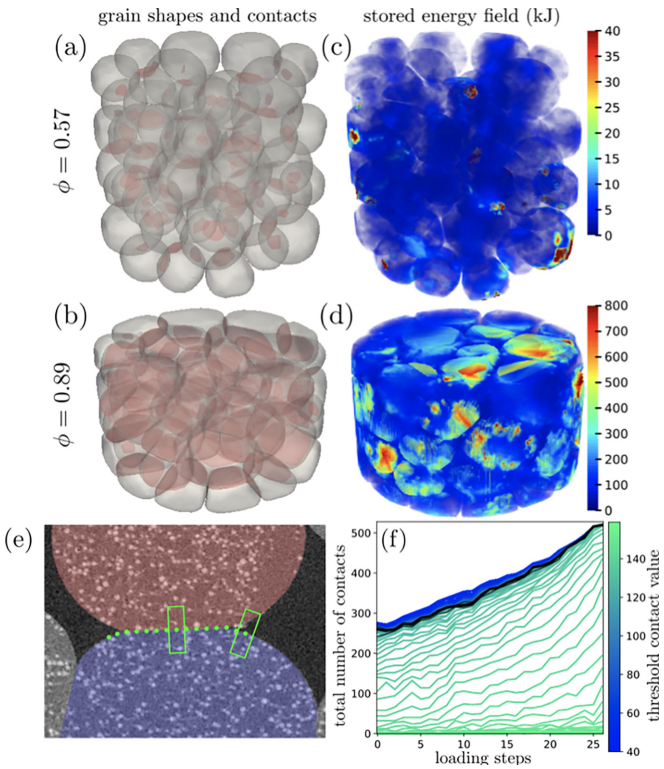

FIG. 2. (a) and (b) Evolution of 3D contours of the particles as obtained from DVC. The contact areas are shown in red. (c) and (d) Corresponding packing showing stored energy density fields. (e) Two-dimensional view of an x-ray slice zoomed in on the contact between two grains. Green dots are potential contact points where the average x-ray density is probed inside the green rectangles. The average value of this density in these subzones constitutes a contact detection threshold. (f) Evolution of the number of contacts in the whole system from varying the threshold on the contact criterion.

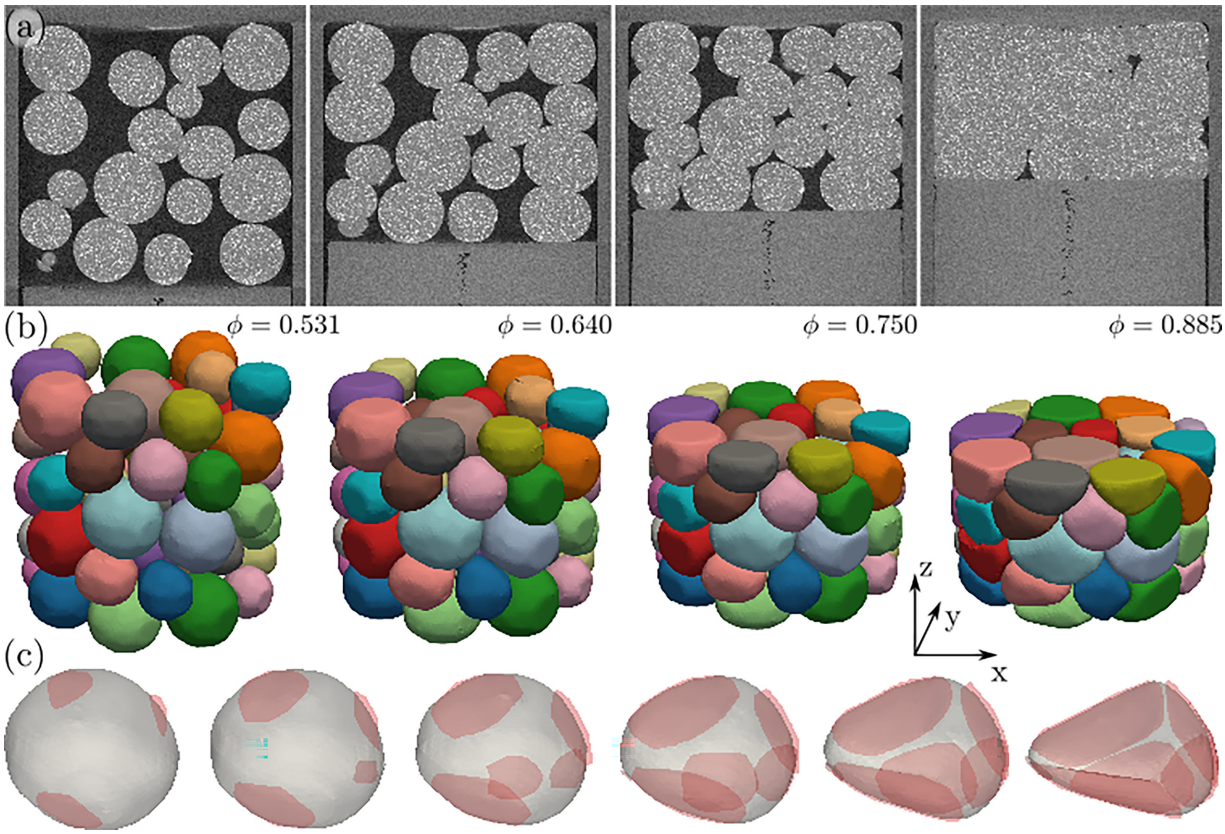

FIG. 3. Raw and postprocessed data. (a) Middle slice of the x-ray scanner density matrix for different levels of compression. The system is compressed vertically from the bottom. (b) Corresponding 3D reconstruction of the particle surfaces from the DVC results obtained from the x-ray scans. (c) Evolution of the shape and contact surfaces (in red) of a given particle when compressed.

cess. To measure contact surfaces, we first discretize the border into a network of points separated by 18 voxels. For each of these points, if it is close to another point belonging to another particle, we extract a parallelepipedic submatrix centered around this point and aligned perpendicularly from the boundary, as shown in Fig. 2(e). We compute the average value of this submatrix. The higher this density value is, the higher the quantity of matter in the submatrix is, so the higher the probability of contact is. In Fig. 2(f) we plot the evolution of the number of contacts for different thresholds of this density value to consider the contact real. We observe that the density of curves increases for a threshold of 120, which is close to the mean density ($2^8/2$). This is the threshold we pick.

III. RESULTS

A. Compaction and connectivity evolution laws

Figures 3(a) and 3(b) show tomographic slices and corresponding 3D reconstructions of one of our samples for different levels of compression: from an initially jammed state to a highly compact one. During the compression process the voids within the assembly are progressively filled due to the deformation of the grains. Meanwhile, the packing fraction ϕ increases from $\phi_0 \approx 0.53$ (jammed state) to $\phi_{\max} \approx 0.9$ for the most compact state obtained. In Fig. 4, deep in the jammed state, we present the evolution of the global vertical strain $\varepsilon = \ln(H/H_0)$, with H_0 being the initial height of the cylinder [blue curve in Fig. 4(a)]; the coordination number Z [black curves in Fig. 4(a)]; and the applied vertical stress P [Fig. 4(b)] as a function of the packing fraction ϕ. Basically, ε decreases as ϕ increases following, with a good approximation, a logarithmic law: $\varepsilon \sim -\ln(\phi/\phi_0)$. The evolution of Z is such that it increases in a nonlinear way with ϕ from $Z_0 \approx 4.5$ to $Z_{\max} \approx 8.5$, as ϕ goes from ϕ_0 to $\phi_{\max}$. As shown in previous 2D numerical and experimental works [12–14,20,22,56] and, more recently, in three dimensions [23], this increase follows a power law with an exponent of 1/2:

$$Z - Z_0 = \xi\sqrt{\phi - \phi_0}, \tag{1}$$

where $\xi \approx 6$ is fitted from experimental data. This power-law fits our 3D experiment [Fig. 4(a), black solid line] quite well, but a better exponent can be found: 2/3 (black dashed line). This implies a difference between experimental and numerical results reminiscent of what has been observed for foam [56]. The small variations from this phenomenological prediction at a high packing fraction are due to the experimental uncertainty in the contact detection when the system is densely packed. In this latter case, we note that the system most likely enters a different regime. Thus, our experimental results confirm the validity of the phenomenological law between Z and ϕ up to a certain density. This law has often been verified only numerically or in 2D model experiments [12–14,20,22,23].

Along with the evolution of Z, the compaction of the assembly is also characterized by the P vs ϕ curves, shown in Fig. 4(b). We find that P slowly increases with ϕ at low density

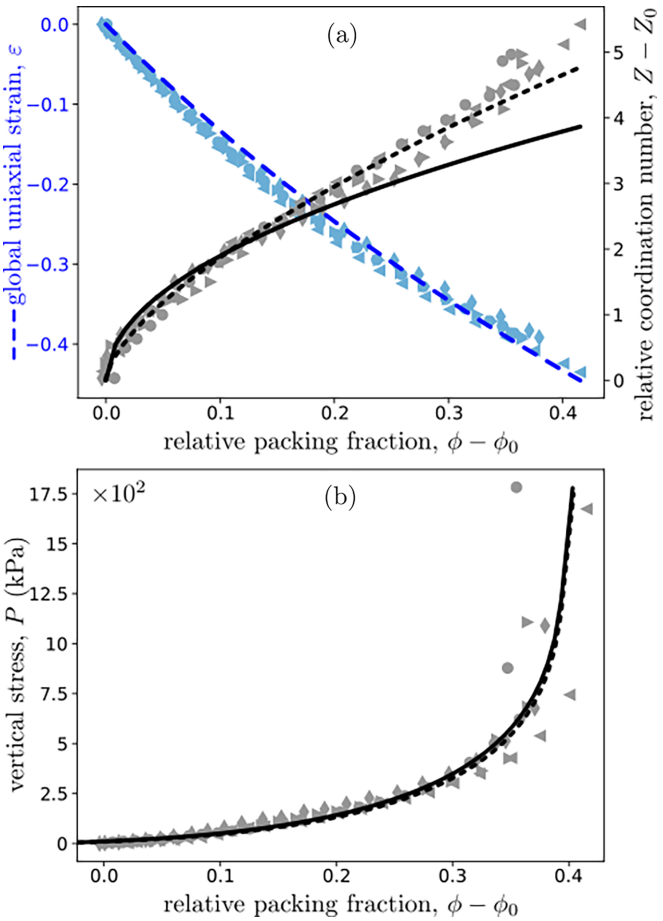

FIG. 4. Macroscopic evolution. (a) Evolution of the global uniaxial strain ε (dashed blue line) and of the coordination number increase from the jamming point $Z - Z_0$ (solid black line) as a function of the relative packing fraction $\phi - \phi_0$. Points are experimental data (different symbols stand for different experiments), while lines are analytical models. The blue dashed line for the global strain is a scaling of $-\ln(\phi/\phi_0)$, while the black solid line is a plot of Eq. (1). The black dashed line is a power law similar to Eq. (1) with an exponent of 2/3. (b) Compaction curve: applied vertical stress P as a function of $\phi - \phi_0$. Points are experimental data, while the solid black line is the analytical model given by Eq. (2). The dashed curve is similar to Eq. (2), but adapted to integrate Eq. (1) with an exponent of 2/3.

and then diverges as the packing fraction tends to $\phi^*_{\max} \approx 1$, the "theoretical" maximum packing fraction. This divergence is expected since the assembly of soft grains begins to behave as a rigid body when the grains almost fill all the voids. By combining the micromechanical formulation of the granular stress tensor [57], its limit for small deformations, and the evolution of the particle connectivity, we deduce the following equation for the compaction curve P vs $\phi - \phi_0$ (see details in the Appendix A):

$$P = E^* \frac{2(1+2\mu_M)}{3\pi\Gamma^{3/2}} \frac{\phi^*_{\max} - \phi_0}{\phi_0^{3/2}} Z\phi(\phi-\phi_0)^{1/2} \times \ln\left(\frac{\phi^*_{\max} - \phi_0}{\phi^*_{\max} - \phi}\right), \quad (2)$$

where $E^* = E/2(1-\nu^2)$ is the reduced Young's modulus, $\mu_M = 0.25$ is related to the macroscopic friction of an assembly of spherical grains, $\Gamma = 3.89$ is a structural parameter linearly relating the macroscopic deformation and the mean contact deflection, and Z is the coordination number given by Eq. (1). The power of the proposed compaction law is that it is based only on physical parameters that are easy to measure experimentally. As we can see, our data are very well fitted by Eq. (2). Also, the exponent of Eq. (1) does not significantly change the shape of this law. This validates a recently introduced micromechanical framework allowing us to design compaction laws for different loading conditions and material properties [22] and extends it to the case of 3D uniaxial compression.

B. Quantitative description of grain shape evolution

The strength of our experimental setup and data postprocessing is obtaining precise information at the grain scale, such as the evolution of grain shape as well as the evolution of the contact geometries when the whole assembly is compacted. For example, Fig. 3(c) shows the evolution of the shape of one of the grains located in the center of the system, which progressively shifts from spherical to a flattened polyhedral shape with increasing contact areas. We define the asphericity parameter by $\alpha = \frac{a_p^{3/2}}{3\sqrt{4\pi}v_p}$, where a_p and v_p are the surface area and volume of a given particle p, respectively. By construction, α equals 1 for a sphere and is higher for any other geometry. $\bar{\alpha}$ is the average of this quantity over all the grains of the packing. Figure 5(b) (green curve) displays the evolution of $\bar{\alpha}$ as a function of the excess of the packing fraction $\phi - \phi_0$. We find that the asphericity increases as a power law: $\bar{\alpha} = 1 + (\phi - \phi_0)^\beta$, with $\beta = 3/2$ and 1 corresponding to the initial asphericity. Interestingly, a similar trend was recently observed in 2D (3D) numerical simulations of compaction of soft disk (sphere) assemblies [23,24]. Thus, our experiments confirm this seemingly universal geometric feature of soft particle compaction.

Above the loss of sphericity it is important to analyze how particles deform. To do so, for each grain, we consider the evolution of its aspect ratio λ and its average orientation ϵ. λ is defined as the ratio of the shortest straight line over the longest straight line joining opposite boundaries of a given grain and crossing its center of mass. Note that, for highly deformed grains, these two axes are not necessarily perpendicular to each other. ϵ is the sinus of θ, the elevation angle of the shortest direction [see Fig. 5(a)]. As observed in Fig. 5(b), the average particle aspect ratio $\bar{\lambda}$ decreases with ϕ from 1 (spherical shape) to values close to 0.6. Meanwhile, their average orientation $\bar{\epsilon}$ increases from 0.5 (anisotropic) to 1 (horizontally expanded) for $\phi \gtrapprox 0.72$. From these observations, a schematic picture emerges to describe the compaction from a grain-scale perspective. The grains elongate in the surrounding voids mainly by increasing the largest distance, contributing to the creation of new contacts aligned along the compression direction. In the other directions, the mean grain aspect ratio also increases by shrinking the shortest length. This is also well evidenced in Fig. 5(c), which shows the average circular profile of the grains. At first this profile is

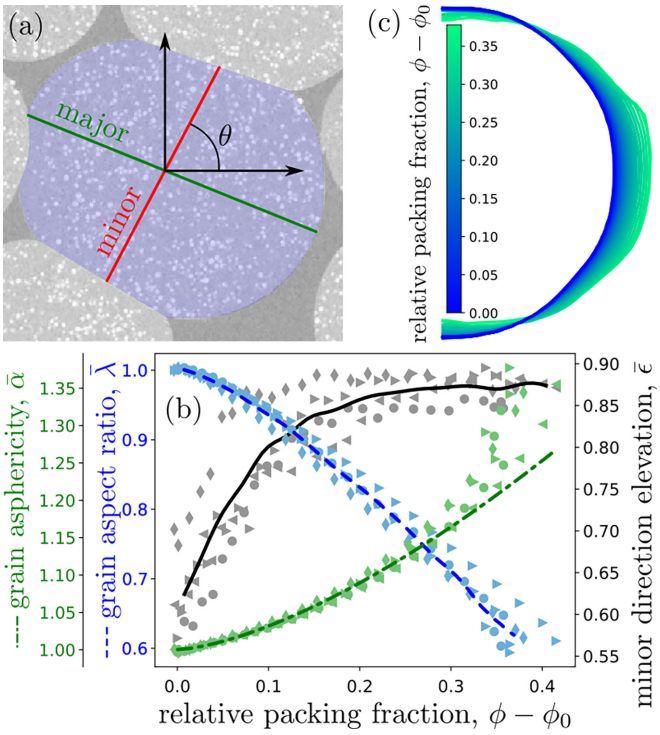

FIG. 5. Grain shape evolution. (a) Schematic view in two dimensions of the major and minor directions of a particle and their orientation with respect to the vertical direction. θ is the elevation angle of the minor direction. (b) Evolution of the mean grain aspect ratio $\bar{\lambda}$ (dashed blue line), of the average of the sinus of the minor direction elevation $\bar{\epsilon}_p$ (black line), and of the average grain asphericity, $\bar{\alpha}$ (dot-dashed green line) as a function of the packing fraction relative to the jamming point $\phi - \phi_0$. Points are experimental data (different symbols stand for different experiments). Blue and black lines are averaged curves, and the green one is the power-law fit: $\bar{\alpha} = 1 + (\phi - \phi_0)^{3/2}$. (c) Evolution of the average shape of the grains as a function of $\phi - \phi_0$. Curves are circumferentially averaged over each grain of the packing.

perfectly semicircular, and it then gets progressively larger in width and thinner in height.

C. Linking contact geometry evolution to packing fraction

Along with the grain shape, the evolution of the contact surface geometries between grains is also probed during the compression. As an illustration, Fig. 6(a) displays the evolution of a typical contact surface within the sample. Qualitatively, close to ϕ_0 the shape of a contact can be considered circular. However, as the compression goes deeper into the jammed state, the contact surface gets larger and exhibits a nontrivial concave shape. As for the grain shape, for each contact, we define the mean contact surface acircularity $\gamma = \frac{p_c^2}{4\pi s_c}$, where p_c and s_c are the perimeter and the surface of this contact, respectively. $\bar{\gamma}$ is the average of this quantity over all the contacts of the packing. In Fig. 6(b) the blue dashed curve shows the evolution of $\bar{\gamma}$ as a function of the excess packing fraction $\phi - \phi_0$. We find that, on average, the contact surfaces can be considered circular up to a fairly high packing fraction, close to 0.83. Before this density $\bar{\gamma} \approx 1$, but beyond,

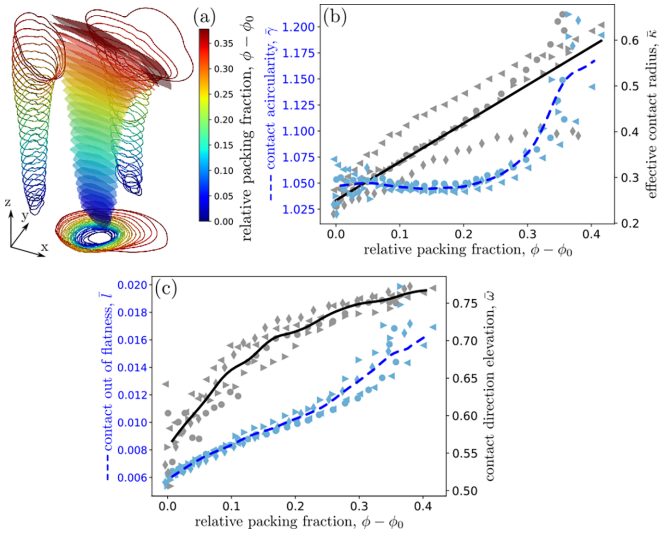

FIG. 6. Contact geometry evolution. (a) Evolution of the shape of a given contact when the system is compressed. Projections of the contact contours on three orthogonal directions are also shown. (b) and (c) Evolution of the average contact acircularity $\bar{\lambda}$ [blue dashed line in (b)], the average effective contact radius $\bar{\kappa}$ [black solid line in (b)], the average contact nonplanarity $\bar{l}$ [blue dashed line in (c)], and the average contact direction elevation $\bar{\omega}$ [black solid line in (c)] as a function of the distance of the packing fraction from the jamming point $\phi - \phi_0$. Points are experimental data (different symbols stand for different experiments), while lines are averaged curves, except the one for $\bar{\kappa}$, which is a linear fit with a slope of 2.94 ± 0.03.

$\bar{\gamma}$ increases suddenly to values close to 1.2. This highlights the strong deviation of the contact surfaces from a circular shape. The shape of this curve is reminiscent of the divergence of P observed in Fig. 4(b). Along with γ, the contact geometry is also characterized by the mean curvature of the contact surfaces l. The latter is defined by the contact nonplanarity, the mean distance between the real contact surface and its average plane. This quantity is then normalized by the mean particle radius R_p. The evolution of its average value $\bar{l}$ as a function of the excess of the packing fraction $\phi - \phi_0$ is shown in Fig. 6(c). We observe that $\bar{l}$ slightly increases with ϕ and remains overall less than 1% of the mean grain radius until, like for $\bar{\gamma}$, a crossover is observed at $\phi \approx 0.83$. Then, a rapid increase is observed, and $\bar{l}$ exceeds more than 1% of the mean grain radius. In other words, from a certain level of compression, the grains indent each other, and the contact surfaces are no longer symmetrical. This leads to concave-shaped contacts, as observed in Fig. 6(a).

To quantify the evolution of the size of the contact, we define the relative effective contact radius $\kappa = \frac{\sqrt{s_c/\pi}}{R_p}$. Using a mean field approach that combines the geometrical properties of a Hertzian contact together with the Z vs ϕ relation [Eq. (1)], we obtain (see details in Appendix B)

$$\bar{\kappa} \propto \phi - \phi_0. \tag{3}$$

We see in Fig. 6(b) that the linear dependence predicted by Eq. (3) is well satisfied up to large ϕ values deep in the

jammed state. However, from $\phi \approx 0.83$, the data slightly deviate from this prediction since the circularity and flatness assumptions of the contact surface are no longer valid. Going further in the contact analysis, in Fig. 6(b) we show the evolution of the mean contact direction $\bar{\omega} = \langle \sin\theta_c \rangle_c$, where θ_c is the elevation angle of the angle normal to the contacts. We find that $\bar{\omega}$ increases from 0.5 (anisotropy) at ϕ_0 to ~0.75 (mainly vertical) for $\phi \to \phi^*_{\max}$. This indicates that the contact surfaces are preferentially oriented perpendicular to the direction of compression as the packing fraction is increased. This is consistent with the preferential direction of grain elongation discussed in the previous section.

D. Deeper within the grains: Strain and energy density fields

The presented method not only allows the measurement of the 3D evolution of grain boundaries but also provides the local displacement field inside each grain, even deep in the jammed state, for highly deformed grains. The right Cauchy-Green deformation [58] tensor and its von Mises norms are deduced from this displacement field [59]. Also, assuming a hyperelastic behavior of the silicone used to make the beads [20,59,60], we compute the energy density stored in the material ρ [20,58]. Figure 7(a) shows the evolution of the mean von Mises strain when the granular system is loaded. We find that the mean von Mises strain first increases linearly with the packing fraction. On average, this implies a proportionality relation between the local and global strains applied to the system.

Still, for a higher packing fraction, from $\phi \approx 0.83$ the local strain enters a regime where it increases more rapidly. In Fig. 6(b), we show the evolution of the average energy density when the system is compressed. This quantity increases quadratically with the packing fraction. This is a direct consequence of the linear relation between the strain and the packing fraction. It implies that even for quite high packing fractions, from a coarse-grained point of view, the system behaves as a solid. Still, when looking at the statistical distribution of the energy field, presented in Fig. 7(c), this analogy is no longer true. Indeed, the probability density function (PDF) of ρ is Gaussian-like for a gently squeezed system, but for more compressed systems, it displays an exponential tail reminiscent of what is observed for the PDF of the interaction forces between rigid grains [7].

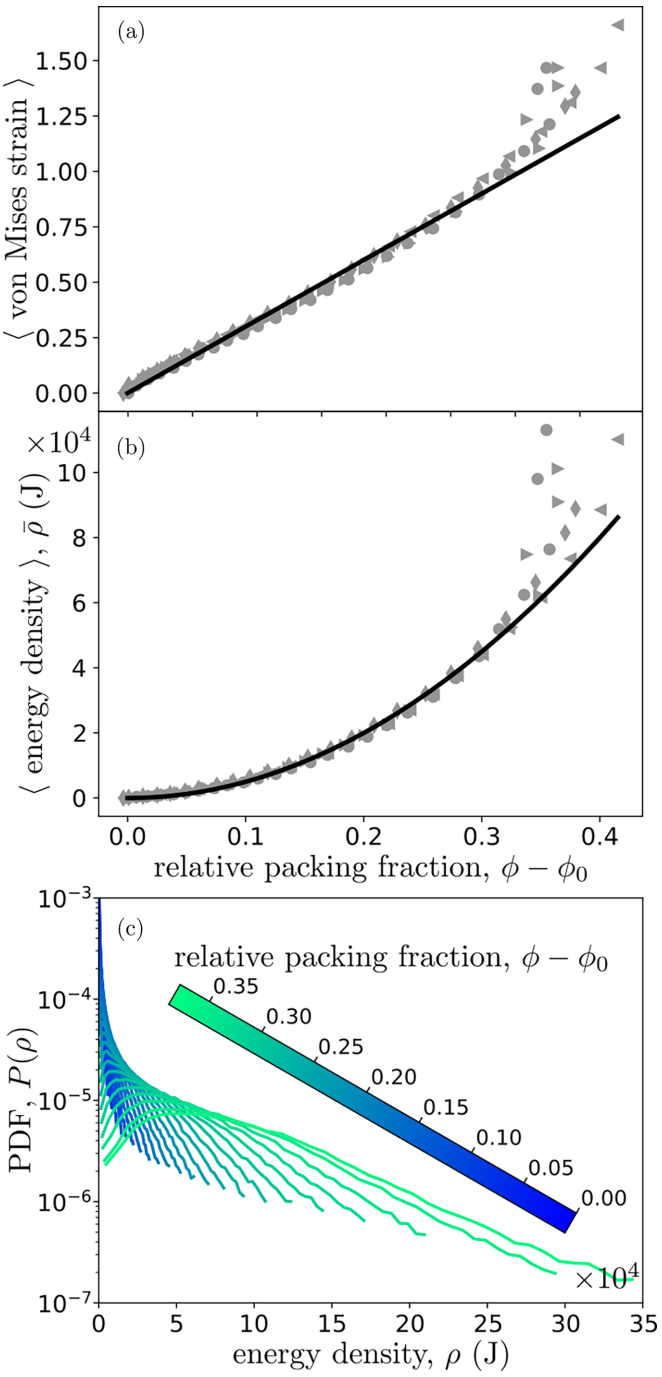

FIG. 7. Local mechanical evolution. Evolution (a) of the average von Mises strain and (b) of the average energy density $\bar{\rho}$ as a function of the distance of the packing fraction from the jamming point $\phi - \phi_0$. Points are experimental data (different symbols stand for different experiments), while in (a) the line shows a linear fit with a slope of 3 ± 0.1 and in (b) the plain curve is the quadratic fit $5 \times 10^5(\phi - \phi_0)^2$. (c) Evolution of the probability density function (PDF) of the energy density $P(\rho)$ when a system is compressed.

IV. DISCUSSION

We have overcome one of the main experimental challenges recently identified as such by the granular matter community [15,61,62]. The experimental framework we presented in this paper permits us to travel from macro- to micro-observables and, conversely, from a highly squeezed granular system deep in the jammed state to a very large packing fraction. The strain tensor in the material of each particle of the whole system was recorded during the compression process, permitting us to compute the evolution of the corresponding stress tensor and energy density. The change in shape of the particles and their contacts were deduced, and the classical—strain vs stress—measurements were also monitored. No classical mechanics observables of the system were kept unknown during the whole loading process, opening the way to a thorough analysis of this complex multiscale mechanical process.

This set of information permitted us to check whether the phenomenological power law between the system

coordination number Z and packing fraction ϕ still holds in three dimensions. Previously, this had been observed only for 2D experiments [12–14,20]. This point extends the domain of validity of this relation and suggests that more contacts are created than what was initially expected. The compaction law linking the pressure applied to the system and its packing fraction, built for 2D systems and in three dimensions for isotropic compression, were extended to the case of uniaxially loaded 3D systems. The strength of this theoretical framework, derived from the micromechanical expression of the granular stress tensor, is based on having only physical parameters that are easy to measure experimentally. Our experimental results outstandingly validate this law even deep in the jammed state. This will permit us to predict with great precision the behavior of a loaded system just by knowing the exact nature of the grains.

Moreover, the results presented in these series of 3D experiments show that the mean contact geometry varies linearly with the packing fraction. Just like for the compaction law, this relation is supported by a mean field approximation developed in the small deformation framework. It is remarkable that even deep in the jammed state, where grains are extremely deformed through multiple contacts and the Hertz contact hypothesis is highly violated [36,60], the mean field analytical framework still holds and gives greatly reliable results. This point is a good omen for finding a unified rheological law describing the mechanical behavior of a system from the jammed state up to a bulk material whatever the loading process is.

Still, by tracking the local strain energy during compression, we revealed that, for a very high packing fraction, a transition from granular-like to continuous-like materials exists. For a packing fraction close to 0.83, the average energy density follow a quadratic law with the packing fraction, and the average strain follows a linear law. The description of these quantities remains complex to describe analytically in these high density regimes. In these regimes the particles are highly distorted to fill the last remaining porosities. This is in agreement with the fact that above $\phi \approx 0.83$, the average particle asphericity also follows a well defined power-law behavior with the packing fraction. Below this threshold the material remains remarkably well described by the material rheology taking granular structure into account; on the contrary, above, it enters a more extreme regime where observables vary abruptly. This point, which has also been observed in two dimensions [24,59], clearly evidences a sharp crossover in the material behavior.

Our experimental framework evidences heuristic and analytical laws linking different observables of densely packed granular systems. This provides insights into the granular micromechanisms and how they are responsible for specific macroscopic behavior. On top of permitting us to predict the evolution of a densely packed system, our findings permit us to deduce the global state of a system through local observations and the converse. This opens new perspectives for rheological analysis of highly deformable grain assemblies in various fields ranging from biology [62–64] to engineering [65] and geophysics [49,50], to name just a few.

ACKNOWLEDGMENTS

We are grateful to G. Camp and S. Devic for helping with the sample preparation.

APPENDIX A: DERIVATION OF THE COMPACTION EQUATION FOR 3D UNIAXIAL GEOMETRY

We briefly recall the main ingredients of the theoretical framework presented in [22,23], and we extend it to fit uniaxial 3D geometry. In this case, P is related to the granular stress tensor through its zz component by $P = \sigma_{zz}$. The granular stress tensor is given by $\boldsymbol{\sigma} = n_c \langle \boldsymbol{f}^{\boldsymbol{c}} \otimes \boldsymbol{\ell}^{\boldsymbol{c}} \rangle_c$ [57], where $\boldsymbol{\ell}^{\boldsymbol{c}}$ is the vector between the centers of the grains and $\boldsymbol{f}^{\boldsymbol{c}}$ is the force vector at a contact c. $n_c = N_c/V$ is the density of contacts, with N_c being the total number of contacts in the volume V. Considering a small particle size distribution around the mean diameter d and with $V_p = (\pi/6)d^3$ being the volume of a sphere p, we obtain $n_c \simeq 3Z\phi/(\pi d^3)$, with $Z = 2N_c/N_p$ being the coordination number. From the definition of σ_{zz} via the principal values of $\boldsymbol{\sigma}$, we get

$$P \simeq \alpha \frac{\phi Z}{\pi} \sigma_\ell, \tag{A1}$$

with $\sigma_\ell = \langle f^c \cdot \ell^c \rangle_c / d^3$ being a measure of the mean contact stress and α being a constant related to various microscopic parameters pertaining to the contact and force network specific to uniaxial compression but hardly accessible by means of experiments. However, theoretical developments [66] have shown that these microscopic parameters can be added together to build the shear strength parameter μ_M of the material, allowing us to write $\alpha \sim 1 + 2\mu_M$. For an assembly of frictional spheres, μ_M is close to 0.25. Note that Eq. (A1) is mostly known in its simpler form [10,57], where μ_M is fixed to zero when considering the mean stress from the trace of $\boldsymbol{\sigma}$.

Close to the jammed state (i.e., in the case of small deformations), assuming that the contact forces follow Hertz's law and verifying that (as discussed in Sec. III D) the macroscopic deformation ε is linearly related to the mean contact deformation $\langle \delta^c/R_p \rangle_c$, with δ^c being the reduction in radius at a contact c (via the parameter $\Gamma \sim 3.8$ measured in our experiments), we can rewrite Eq. (A1) as $P_{SD} = -\alpha \frac{2E^*}{3\pi\Gamma^{3/2}} Z_0 \phi \ln^{(3/2)}(\frac{\phi}{\phi_0})$. Now, deep in the jammed state, we rely on the macroscopic hypothesis formulated by Carroll and Kim [32]. Using an analogy between the compaction process and the collapse of a cavity within an elastic medium, they showed that, necessarily, $P \propto \ln[(\phi^*_{\max} - \phi)/(\phi^*_{\max} - \phi_0)]$. By combining this large deformation approach with the small one and Eq. (A1), the compaction equation becomes the one presented in Sec. III A.

APPENDIX B: PREDICTING THE LINEARITY BETWEEN $\bar{l}$ AND ϕ

First, let us remark that $\bar{l}$ can be rewritten as a mean over all grains and contacts: $\bar{l} \sim Z r_c/R_p$. Then, since we have verified (see Sec. III A) that $(\phi - \phi_0)/\phi_0 \sim \varepsilon$ and also that $\varepsilon \sim \langle \delta^c/R_p \rangle_c$ (see Sec. III D), we get the following proportionality between Z and δ: $Z \sim \sqrt{\delta/R_p}$. Finally, from the Hertz theory we get that the radius of the contact surface between two

spheres touching at a contact c is given by $r_c \sim \sqrt{R^* \delta^c}$, with $R^* \equiv R_p$ being the effective radius and δ^c being the reduction in radius at the contact. Injecting the two above proportionalities into the definition of $\bar{l}$ leads to $\bar{l} \sim \sqrt{\delta}\sqrt{\delta} \sim \phi - \phi_0$.

[1] A. J. Liu and S. R. Nagel, Nature (London) **396**, 21 (1998).
[2] D. Bi, J. Zhang, B. Chakraborty, and R. P. Behringer, Nature (London) **480**, 355 (2011).
[3] R. P. Behringer and B. Chakraborty, Rep. Prog. Phys. **82**, 012601 (2019).
[4] D.-H. Nguyen, E. Azéma, F. Radjai, and P. Sornay, Phys. Rev. E **90**, 012202 (2014).
[5] M. V. Hecke, J. Phys.: Condens. Matter **22**, 033101 (2010).
[6] A. Kyrylyuk and A. Philipse, Phys. Status Solidi A **208**, 2299 (2011).
[7] F. Radjai, M. Jean, J.-J. Moreau, and S. Roux, Phys. Rev. Lett. **77**, 274 (1996).
[8] J. F. Peters, M. Muthuswamy, J. Wibowo, and A. Tordesillas, Phys. Rev. E **72**, 041307 (2005).
[9] H. A. Makse, N. Gland, D. L. Johnson, and L. M. Schwartz, Phys. Rev. Lett. **83**, 5070 (1999).
[10] I. Agnolin and J.-N. Roux, Phys. Rev. E **76**, 061304 (2007).
[11] M. H. Khalili, J.-N. Roux, J.-M. Pereira, S. Brisard, and M. Bornert, Phys. Rev. E **95**, 032908 (2017).
[12] D. J. Durian, Phys. Rev. Lett. **75**, 4780 (1995).
[13] T. S. Majmudar, M. Sperl, S. Luding, and R. P. Behringer, Phys. Rev. Lett. **98**, 058001 (2007).
[14] G. Katgert and M. van Hecke, Europhys. Lett. **92**, 34002 (2010).
[15] J. Barés, M. Cárdenas-Barrantes, D. Cantor, M. Renouf, and E. Azéma, Pap. Phys. **14**, 140009 (2022).
[16] D. Cantor, M. Cárdenas-Barrantes, and L. F. Orozco, Pap. Phys. **14**, 140007 (2022).
[17] B. Harthong, D. Imbault, and P. Dorémus, J. Mech. Phys. Solids **60**, 784 (2012).
[18] Q. Ku, J. Zhao, G. Mollon, and S. Zhao, Powder Technol. **421**, 118455 (2023).
[19] N. Abdelmoula, B. Harthong, D. Imbault, and P. Dorémus, J. Mech. Phys. Solids **109**, 142 (2017).
[20] T.-L. Vu, J. Barés, S. Mora, and S. Nezamabadi, Phys. Rev. E **99**, 062903 (2019).
[21] S. Nezamabadi, X. Frank, J.-Y. Delenne, J. Averseng, and F. Radjai, Comput. Phys. Commun. **237**, 17 (2019).
[22] D. Cantor, M. Cárdenas-Barrantes, I. Preechawuttipong, M. Renouf, and E. Azéma, Phys. Rev. Lett. **124**, 208003 (2020).
[23] M. Cárdenas-Barrantes, D. Cantor, J. Barés, M. Renouf, and E. Azéma, Soft Matter **18**, 312 (2022).
[24] M. Cárdenas-Barrantes, J. Barés, M. Renouf, and E. Azéma, Phys. Rev. E **106**, L022901 (2022).
[25] M. Cárdenas-Barrantes, D. Cantor, J. Barés, M. Renouf, and E. Azéma, Phys. Rev. E **103**, 062902 (2021).
[26] D. Howell, R. P. Behringer, and C. Veje, Phys. Rev. Lett. **82**, 5241 (1999).
[27] K. E. Daniels and N. W. Hayman, J. Geophys. Res. **113**, B11411 (2008).
[28] A. Le Bouil, A. Amon, S. McNamara, and J. Crassous, Phys. Rev. Lett. **112**, 246001 (2014).
[29] J. Barés, D. Wang, D. Wang, T. Bertrand, C. S. O'Hern, and R. P. R. P. Behringer, Phys. Rev. E **96**, 052902 (2017).
[30] M. Cárdenas-Barrantes, D. Cantor, J. Barés, M. Renouf, and E. Azéma, Phys. Rev. E **102**, 032904 (2020).
[31] E. E. Walker, Trans. Faraday Soc. **19**, 73 (1923).
[32] M. M. Carroll and K. T. Kim, Powder Metall. **27**, 153 (1984).
[33] J. Secondi, Powder Metall. **45**, 213 (2002).
[34] J. M. Montes, F. G. Cuevas, J. Cintas, and Y. Torres, Granular Matter **12**, 617 (2010).
[35] L. Parilak, E. Dudrova, R. Bidulsky, and M. Kabatova, Powder Technol. **322**, 447 (2017).
[36] L. D. Landau, E. M. Lifshitz, A. M. Kosevich, and L. P. Pitaevskii, *Theory of Elasticity*, Vol. 7 (Elsevier, 1986).
[37] J. Brujić, S. F. Edwards, D. V. Grinev, I. Hopkinson, D. Brujić, and H. A. Makse, Faraday Discuss. **123**, 207 (2003).
[38] N. Brodu, J. A. Dijksman, and R. P. Behringer, Nat. Commun. **6**, 6361 (2015).
[39] K. E. Daniels, J. E. Kollmer, and J. G. Puckett, Rev. Sci. Instrum. **88**, 051808 (2017).
[40] A. A. Zadeh, J. Barés, T. A. Brzinski, K. E. Daniels, J. Dijksman, N. Docquier, H. O. Everitt, J. E. Kollmer, O. Lantsoght, D. Wang *et al.*, Granular Matter **21**, 83 (2019).
[41] P. Jongchansitto, X. Balandraud, I. Preechawuttipong, J.-B. L. Cam, and P. Garnier, Exp. Mech. **58**, 1469 (2018).
[42] E. Marteau and J. E. Andrade, Granular Matter **19**, 77 (2017).
[43] Y. Wang, J. Shang, Y. Wang, and J. Zhang, Phys. Rev. Res. **3**, 043053 (2021).
[44] F. Fazelpour, Z. Tang, and K.-E. Daniels, Soft Matter **18**, 1435 (2022).
[45] M. Saadatfar, A. Sheppard, T. Senden, and A. J. Kabla, J. Mech. Phys. Solids **60**, 55 (2012).
[46] M. Wiebicke, E. Andò, I. Herle, and G. Viggiani, Meas. Sci. Technol. **28**, 124007 (2017).
[47] B. Indraratna, Y. Qi, T. Ngo, C. Rujikiatkamjorn, B.-F. Neville, and A. Shahkolahi, Geosciences **9**, 30 (2019).
[48] W. Tsoi and K. Lee, Géotechnique **61**, 133 (2011).
[49] H.-H. Tsang, Earthquake Eng. Struct. Dyn. **37**, 283 (2008).
[50] A. Tsiavos, N. A. Alexander, A. Diambra, E. Ibraim, P. J. Vardanega, A. Gonzalez-Buelga, and A. Sextos, Soil Dyn. Earthquake Eng. **125**, 105731 (2019).
[51] M. Mashiri, J. Vinod, M. N. Sheikh, and H.-H. Tsang, Soils Found. **55**, 517 (2015).
[52] S. Mukhopadhyay and J. Peixinho, Phys. Rev. E **84**, 011302 (2011).
[53] SORTA-Clear 18, castable silicone from Smooth-On, https://www.smooth-on.com/products/sorta-clear-18/.
[54] G. Viggiani, E. Andò, D. Takano, and J. C. Santamarina, Geotech. Test. J. **38**, 61 (2015).
[55] L. A. Feldkamp, L. C. Davis, and J. W. Kress, J. Opt. Soc. Am. A **1**, 612 (1984).
[56] G. Katgert, B. P. Tighe, and M. van Hecke, Soft Matter **9**, 9739 (2013).
[57] B. Andreotti, Y. Forterre, and O. Pouliquen, *Granular Media: Between Fluid and Solid* (Cambridge University Press, Cambridge, 2013).
[58] L. A. Taber, *Nonlinear Theory of Elasticity: Applications in Biomechanics* (World Scientific, Singapore, 2004).
[59] T.-L. Vu and J. Barés, Phys. Rev. E **100**, 042907 (2019).

[60] T.-L. Vu, J. Barés, S. Mora, and S. Nezamabadi, Exp. Mech. **59**, 453 (2019).
[61] M. Schröter, C. Lyv, J. Huang, and K. Huang, Pap. Phys. **14**, 140015 (2022).
[62] M. L. Manning, Phys. Rev. Lett. **130**, 130002 (2023).
[63] M. Czajkowski, D. Bi, M. L. Manning, and M. C. Marchetti, Soft Matter **14**, 5628 (2018).
[64] L. Yan and D. Bi, Phys. Rev. X **9**, 011029 (2019).
[65] A. R. Cooper and L. E. Eaton, J. Am. Ceram. Soc. **45**, 97 (1962).
[66] H. Ouadfel and L. Rothenburg, Mech. Mater. **33**, 201 (2001).